AMERICAN SOCIETY FOR MICROBIOLOGY | mSphere®

RESEARCH ARTICLE
Host-Microbe Biology

Label-Free Digital Holo-tomographic Microscopy Reveals Virus-Induced Cytopathic Effects in Live Cells

Artur Yakimovich,[a,b] Robert Witte,[a] Vardan Andriasyan,[a] Fanny Georgi,[a] Urs F. Greber[a]

[a]Department of Molecular Life Sciences, University of Zurich, Zurich, Switzerland
[b]MRC Laboratory for Molecular Cell Biology, University College London, London, United Kingdom

ABSTRACT Cytopathic effects (CPEs) are a hallmark of infections. CPEs are difficult to observe due to phototoxicity from classical light microscopy. We report distinct patterns of virus infections in live cells using digital holo-tomographic microscopy (DHTM). DHTM is label-free and records the phase shift of low-energy light passing through the specimen on a transparent surface with minimal perturbation. DHTM measures the refractive index (RI) and computes the refractive index gradient (RIG), unveiling optical heterogeneity in cells. We find that vaccinia virus (VACV), herpes simplex virus (HSV), and rhinovirus (RV) infections progressively and distinctly increased RIG. VACV infection, but not HSV and RV infections, induced oscillations of cell volume, while all three viruses altered cytoplasmic membrane dynamics and induced apoptotic features akin to those caused by the chemical compound staurosporine. In sum, we introduce DHTM for quantitative label-free microscopy in infection research and uncover virus type-specific changes and CPE in living cells with minimal interference.

IMPORTANCE This study introduces label-free digital holo-tomographic microscopy (DHTM) and refractive index gradient (RIG) measurements of live, virus-infected cells. We use DHTM to describe virus type-specific cytopathic effects, including cyclic volume changes of vaccinia virus infections, and cytoplasmic condensations in herpesvirus and rhinovirus infections, distinct from apoptotic cells. This work shows for the first time that DHTM is suitable to observe virus-infected cells and distinguishes virus type-specific signatures under noninvasive conditions. It provides a basis for future studies, where correlative fluorescence microscopy of cell and virus structures annotate distinct RIG values derived from DHTM.

KEYWORDS apoptosis, cell contraction, cell volume, herpes simplex virus, label-free microscopy, live-cell microscopy, membrane blebbing, refractive index, rhinovirus, tomography, vaccinia virus, virus infection

Viruses have a dual nature, the particle and the infected cell. At the onset of an infection, the particle introduces proteins, DNA or RNA, and sometimes lipids into the host cell. The infected cell either produces viral components that are encoded in the viral genome or raises an immune reaction against the virus and silences the infection. In the former case, the infected cell develops a cytopathic effect (CPE). CPEs are diagnostic hallmarks of a particular virus, and it is well-known that CPEs occur in cell cultures (for reviews, see references 1 and 2). CPE can predict clinical outcomes *in vivo*. Examples include exacerbation of steatosis by hepatitis C virus, apoptosis in trigeminal ganglia by herpes simplex virus (HSV), or aseptic meningitis, paralysis, cardiomyelitis, and herpangina by enteroviruses, including poliovirus, coxsackievirus, and enterovirus (EV) type 71 (3–5). While virus-induced CPE and cell death are exacerbated by cytokine responses, cytotoxic T cells, or natural killer (NK) cells, virus-induced CPE of cultured cells apparently proceeds in a cell-autonomous manner.

Received 2 November 2018 **Accepted** 5 November 2018 **Published** 21 November 2018

Citation Yakimovich A, Witte R, Andriasyan V, Georgi F, Greber UF. 2018. Label-free digital holo-tomographic microscopy reveals virus-induced cytopathic effects in live cells. mSphere 3:e00599-18. https://doi.org/10.1128/mSphereDirect.00599-18.

Editor Michael J. Imperiale, University of Michigan—Ann Arbor

Copyright © 2018 Yakimovich et al. This is an open-access article distributed under the terms of the Creative Commons Attribution 4.0 International license.

Address correspondence to Urs F. Greber, urs.greber@imls.uzh.ch.

A.Y. and R.W. contributed equally to this work.

Solicited external reviewers: Jacomine Krijnse Locker, Institut Pasteur; Craig Cameron, Pennsylvania State University.

This paper was submitted via the mSphereDirect™ pathway.

Label-free digital holo-tomographic microscopy across cells in 3 dimensions reveals virus-specific features, including periodic cell volume changes, and cytoplasmic membrane dynamics for vaccinia virus, herpesvirus, and rhinovirus @ayakimovich.

The nature and the extent of CPE depend on the virus, cell type, host innate response, and progression of infection. For example, distinct levels of CPE correlate with the amounts of newly synthesized virus particles (6). In adenovirus-infected cells, the cells may lyse and release large amounts of viral particles after the cells show strong CPEs, while persistently infected cells produce small amounts of progeny over time (long term) and have weak CPEs (7, 8). Yet, the extent of CPE does not always correlate with virion production, as cells undergoing programmed cell death feature strong CPE at low viral titers (9–11). As viruses hijack cellular resources, CPEs elicited by virus infection may have distinct features, such as loss of membrane integrity, cell shrinkage, increased chromatin density, cell detachment from the substratum, formation of syncytia, loss or enforcement of the cytoskeleton, and reorganization of intracellular membranes (2, 12, 13). Despite the predictive nature of CPE for clinical and biological infections, time-resolved 3D analyses of virus-induced CPE are missing.

Here we describe a new approach using 3D digital holo-tomographic microscopy (DHTM) to study the CPEs induced by three different viruses: vaccina virus (VACV), a large DNA virus replicating in the cytoplasm, herpes simplex virus type 1 (HSV-1), a large DNA virus replicating in the nucleus, and rhinovirus (RV), a small RNA virus replicating on cytoplasmic membranes. Classical video-enhanced contrast optical microscopy, such as interference microscopy and bright-field microscopy, are limited by uneven image field intensity, lack of tomographic information, and a focus-dependent size inflation of structures due to diffraction limitation (14). In contrast, DHTM allows prolonged quantitative time-resolved 3D image acquisition using an ultralow-powered laser (520-nm class 1 with 0.2 mW/mm^2) without recognizable phototoxicity at high temporal and spatial resolution (15).

RESULTS

We infected HeLa cells with the VACV strain Western Reserve harboring an early/late GFP expressed transgene (VACV_WR E/L-GFP [VACV-GFP]) at a multiplicity of infection (MOI) of 2, yielding >95% infected cells, fixed the cells 8 h postinfection (pi) with paraformaldehyde, and recorded the refractive index (RI), nuclear DAPI stain, and GFP intensity by correlative DHTM and fluorescence microscopy and compared the infected cells to noninfected cells. At 8 h pi, all cells inoculated with VACV-GFP were infected based on their GFP intensity and DAPI staining of cell nuclei, whereas the GFP intensity of the uninfected cells was in the range of the background (Fig. 1A). Based on the RI change across a volume, the RI gradient (RIG) can be computed across the whole cell, similar to the RIG across an index gradient lens (for a simplistic illustration, see Fig. 1B and C).

We next imaged VACV-GFP-infected and uninfected cells in live-cell mode by DHTM in 2-h intervals for up to 8 h pi (Fig. 2A). For each condition, two dishes were infected as described in Materials and Methods. At least five randomly chosen cells from each dish were imaged, yielding at least 10 cells per time point and condition. A progressive and prominent change in RI was observed in the infected cells, visualized in scaled pseudocolor. In contrast, the uninfected cells and the VACV-GFP-infected cells treated with the deoxynucleoside analogue cytarabine (AraC), an inhibitor of VACV late gene expression (16, 17), showed less prominent RI changes, although AraC-treated cells inoculated with VACV-GFP exhibited a strong increase in RI in the cell nucleus. We quantified the RI change by deriving the RIG values across the entire cell (Fig. 2B), as described in Materials and Methods. The RIG values of the VACV-GFP-infected cells gradually increased as the infection progressed, reaching threefold at 8 h pi compared to the RIG prior to infection. In contrast, the RIG values of uninfected cells remained largely constant over 8 h. The AraC-treated cells showed only a small RIG increase of about 1.3-fold, suggesting that the RIG increase is predominantly due to viral late gene expression. VACV infections exhibit membrane blebbing phenotypes at early and late time points, as well as focal bud-like swellings (18). Such features are diagnostic of a contractile cell cortex, as reported for uninfected cells in cell migration and response to mechanical cues (19). We noticed an increased fraction of blebbing cells over 2 to 8 h

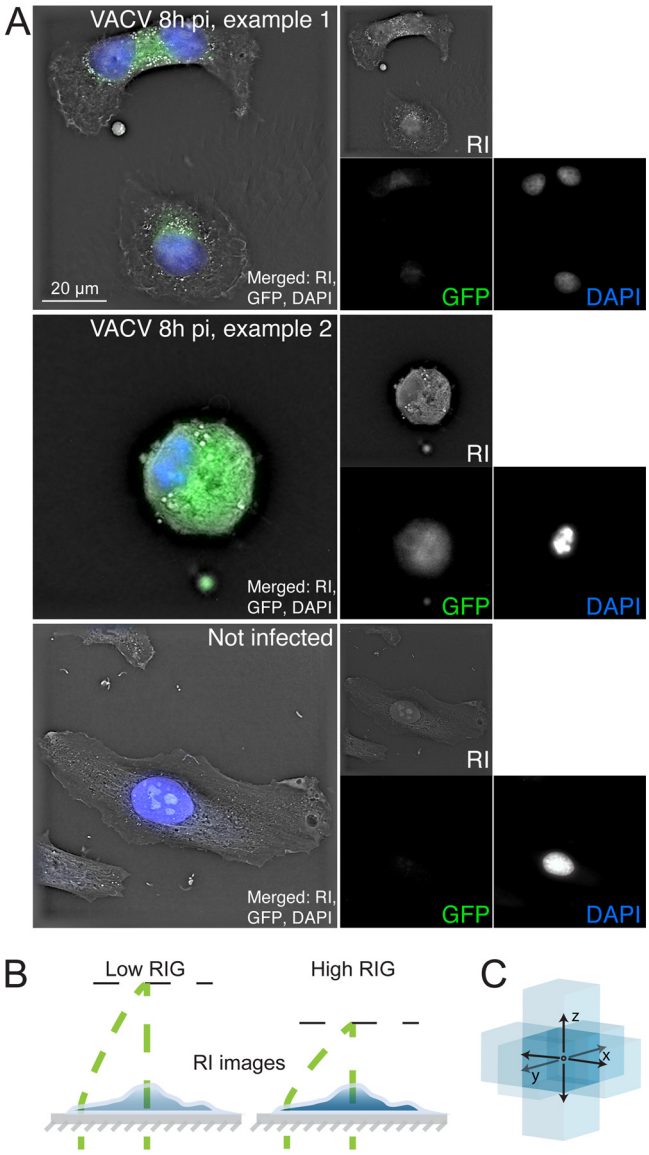

FIG 1 Correlative digital holo-tomographic microscopy and light microscopy of fixed and permeabilized cells. (A) Representative images of HeLa-ATCC cells incubated with 2 ml RPMI at 37°C for 8 h, fixed in 4% PFA in PBS, and imaged with a DHTM microscope and an attached epifluorescence module. The cells were either infected with VACV expressing GFP under the control of early/late promoters (VACV_E/L-GFP; top and middle panels) at an MOI of 2 or left uninfected (bottom panel). The top panels depict a VACV-GFP-infected cell in early infection stage. The middle panels depict a rounding cell, indicating late-stage VACV infection. The bottom panel depicts an uninfected cell. RI is displayed in gray, GFP is shown in green, and nuclei stained with DAPI appear in blue. Bar, 20 μm. (B) Schematic illustrations of RI computation. A cell can be thought of as a gradient index microlens, changing its optical properties depending on biochemical activities. (C) RIG is derived from RI and represents a voxel-based measurement of the difference of the refractive index in 3D space. The RIG value of the voxel in the middle is represented as a middle blue box, which is calculated based on the difference to the light blue voxels in the 3D neighborhood. Note that the reference beam (curved green dashed line) does not pass through the sample. RI is based on changes between the beam (straight green dashed line) and the reference beam.

pi in the presence of AraC (Fig. 2C). This is distinct from membrane blebbing during entry (20) and suggests that blebbing at 8 h pi does not require viral late gene expression and does not affect the RIG.

To test whether similar morphology changes of the VACV-GFP-infected cells can be observed with an alternative imaging modality, we infected HeLa cells with VACV-GFP at an MOI of 2 and imaged live cells in phase-contrast and fluorescence modes at 5-min

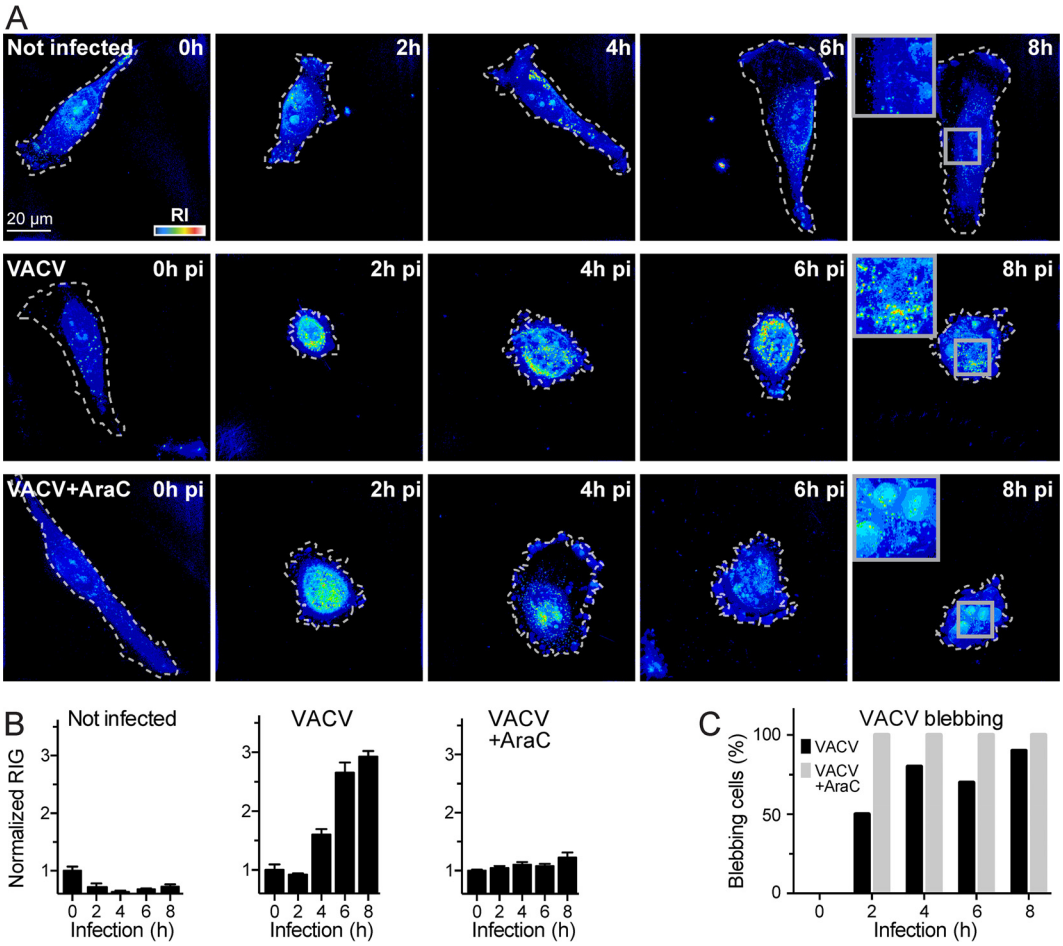

FIG 2 VACV late gene expression increases the cellular RIG. (A) Representative images of HeLa-ATCC cells incubated with 2 ml RPMI at 37°C for 8 h and imaged at 2-h intervals by DHTM. Cells were uninfected, infected with VACV-GFP at an MOI of 2, or infected with VACV-GFP at an MOI of 2 in the presence of 10 μM AraC. The perimeters of the cells grown on coverslips are outlined with white dashed lines. RIs are depicted as intensity values in a "thermal" lookup table. Images were obtained as holograms and depicted as projections of maxima along the *z* axis of the 3D stacks. Bar, 20 μm. (B) Cell RIG quantification of panel A. RIG values were normalized to 1 for 0 h postinfection (pi). Bars depict mean values plus SEM (error bars) of at least 10 cells for each condition and time point. (C) Comparison of the frequency of the "blebbing" phenotype in VACV-GFP-infected cells and VACV-GFP-infected cells in RPMI containing 10 μM AraC. Data from at least 10 cells per time point and condition were acquired and manually scored as blebbing or nonblebbing.

intervals for 8 h (Fig. 3; see also Video S1 in the supplemental material) by using a high-throughput light microscope. In agreement with the DHTM imaging results, the VACV-GFP-infected cells expressed the GFP transgene at increasing intensity over the course of infection. As recorded in the DHTM experiments, we observed host cell rounding, contractions and late stage blebbing of the infected cells, while the features of the uninfected cells remained largely invariant.

We next investigated the dynamic properties of the VACV-GFP-infected cells by using the holographic information, including cell volume. We reasoned that a change in cell volume might result in changes in the density of the cytoplasm, and hence affect the refractive properties of the cell. The accuracy of volumetric measurements based on DHTM was first assessed with polystyrene beads of different nominal sizes ranging from 0.5 to 4 μm (Fig. 4A). Bead size was determined by two different analysis methods, a pixel-based method using the vendor's software, STEVE, and an object-based 3D-surface segmentation method using Imaris (Fig. 4B). Both procedures yielded similar results, although the object-based method was slightly more accurate.

To measure cell volume by DHTM, we used the image stack segmentation procedure in Imaris. Time-resolved 3D live-cell DHTM imaging of infected and uninfected

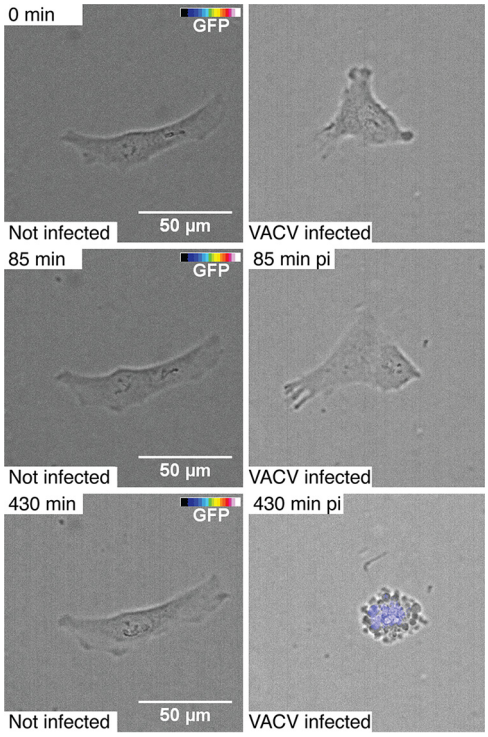

FIG 3 Cell morphology and VACV-GFP transgene expression visualized by automated and correlative phase-contrast and fluorescence live-cell time-lapse microscopy. HeLa-ATCC cells were uninfected (left panels) or infected (right panels) with VACV-GFP using the cold binding protocol (30-min inoculation on ice, wash, and transfer to 37°C). Cells were imaged with a high-throughput wide-field microscope every 5 min for 8 h. Cells were visualized with transmission light, the GFP fluorescence was intensity color coded (color bar ranging from transparent through blue to white). Bars, 50 μm. See also Video S1 in the supplemental material.

cells between 0 and 8 h pi indicated that the VACV-GFP-infected cells underwent a series of shrinkage and dilation phases, while the volume of the uninfected cells remained largely constant (Fig. 5, Video S2, and Video S3). The first shrinkage phase peaked at about 100 min pi and reduced the cell volume by about 50%. This contraction was followed by a steady recovery phase restoring the original volume at about 180 min pi. The next shrinkage period started at 230 min and lasted about 40 min, followed by a short recovery phase of about 30 min, and a period of stable volume with minor fluctuations until 440 min pi, when another shrinkage period occurred. We did not detect a correlation between cell shrinkage or expansion with the RIG values, the latter steadily increasing over the course of infection. We conclude that the VACV-GFP infection-induced RIG increase is not caused by generic changes in cell volume.

To further explore the correlations of RIG and virus-induced CPE, we recorded RIG in cells infected with HSV-1-GFP harboring a GFP transgene under the constitutively active CMV promoter, and RV-A1a at 0, 8, 10, 12, 14, and 16 h pi (Fig. 6A). Calculations are based on at least 10 cells per time point and condition. In HSV-1-GFP-infected cells, CPE was observed from 8 to 10 h pi on, followed by cell surface roughening at 16 h pi. Remarkably, RIG did not increase despite the onset of CPE prior to 16 h pi (Fig. 6B). Cells infected with RV-A1a showed strong CPE starting from 10 and 12 h pi, involving the condensation of cytoplasm. The RIG of RV-A1a-infected cells steadily increased at 10 to 16 h pi up to about 2.5-fold of the RIG of the uninfected controls. The RIG increase occurred during a time frame when apoptosis, virus-controlled necroptosis, and the loss of cytoskeletal elements, such as F-actin, take place (21–23). Remarkably, RV-A1a-infected cells adopted a transient branched shape at 12 to 14 h pi, before rounding up at 16 h pi (Fig. 6A).

Two distinct inhibitors of RV replication were employed to test whether the RIG

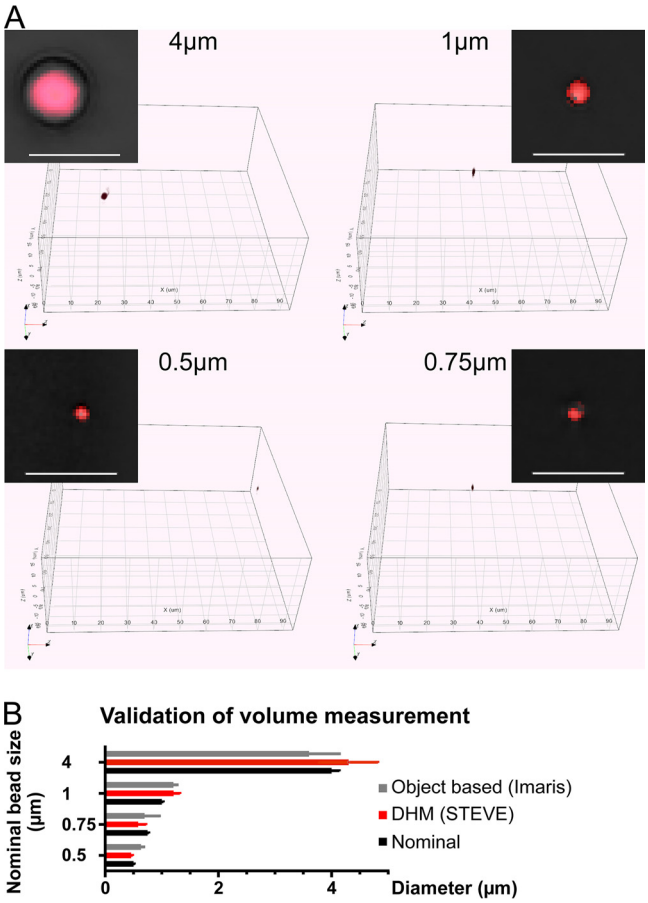

FIG 4 Benchmarking the volume measurement using polystyrene beads of defined size. (A) Polystyrene beads (Tetraspeck; ThermoFisher) of defined diameter were diluted in PBS, allowed to sediment to the bottom of the dishes, and imaged using a 3D Cell Explorer microscope. The small colored boxes depict digital RI stain of beads in red on black background. The large boxes show full 3D visualization of acquired holographs. 3D stacks of the beads were digitally stained (voxel segmented) for an RI estimated to cover at least 95% of the bead volumes. Bars, 5 μm. (B) Comparison of volume quantification performed by voxel summation either by voxel segmentation and counting in STEVE software or by surface fitting in Imaris. Bead diameter was computed based on voxel counts and voxel size and compared to the nominal diameter provided by the manufacturer.

increase was directly associated with RV-A1a replication. The first inhibitor, PIK-93, blocks phosphatidylinositol-4-kinase class 3beta (PI4K3b) activity, and thereby precludes the lipid remodeling by countercurrent lipid fluxes for virus replication (24). In the absence of PI4K3b activity, viral replication is suppressed, because the altered lipid composition of the replication membrane can no longer support viral host proteins necessary for virus replication (reviewed in reference 25). The second inhibitor, MLN9708, is a second-generation inhibitor of the proteasome, which is required for enterovirus replication (26–28). Both PIK-93 and MLN9807 blocked the appearance of high-RI/RIG structures, although the effect of PIK-93 was incomplete (Fig. 7). The partial effect of PIK-93 on RIG was, however, consistent with the partial reduction of PI4P levels and the incomplete inhibition of RV-A1a replication (24, 29). These results support the notion that an increase in RIG in virus-infected host cells occurs in a virus type-specific manner and that RIG changes are a reliable indicator of early and late CPE. The latter is often associated with virus-induced apoptosis, necrosis, or necroptosis. We therefore tested whether the apoptosis-inducing agent staurosporine (30) also induced a RIG response. DHTM tomography of cells treated with 10 μM staurosporine (Fig. 8A) confirmed that staurosporine induces an apoptotic phenotype as early as 1 h after treatment. Image quantifications indicated that RIG increased up to 4 h after applica-

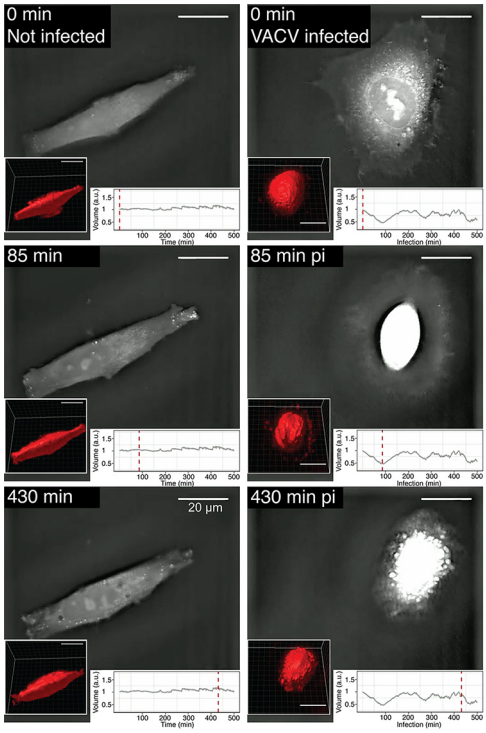

FIG 5 Cell morphology and volume dynamics of VACV-GFP-infected cells, visualized by label-free time-lapse DHTM. HeLa-ATCC cells were infected by VACV-GFP following the cold binding protocol. Cell holograms were acquired every minute for 8 h. RI is shown as gray scale images. Volume measurement was performed using Imaris software by surface fitting and 3D rendering (see the lower left corner of each frame). The plots in the lower right-hand corners show the relative volume (in arbitrary units [a.u.]) normalized to 0 min pi. The red dashed lines correspond to the time points related to the corresponding hologram. Bars, 20 μm. See also Video S2 and Video S3 in the supplemental material.

tion and slightly decreased at 5 h (Fig. 8B). The extent of the RIG increase reached levels similar to the levels reached upon RV-A1a infection, thereby confirming that apoptotic phenotypes can be tracked by DHTM.

DISCUSSION

DHTM is a noninvasive label-free light microscopy technology. It measures the RI of a transparent object by an interference procedure (31–36). DHTM is superior to classical optical techniques, such as tomographic phase microscopy and diffraction phase microscopy (37), because of its high sensitivity, accuracy, and noninvasiveness. The system produces quantitative 3D information at high spatial and temporal resolution. It readily measures the volume of cells and subcellular structures. Furthermore, it can be used to acquire two new dimensions of cell data, RI and RIG, which cannot be readily assessed by other imaging modalities. The methodology is robust and overcomes a series of technical limitations in live-cell pathogen imaging, including the labeling of cellular and viral entities by chemical or genetically encoded fluorophores, and toxicity ensuing imaging (for recent reviews, see references 38 and 39). The noninvasiveness and low laser power required for DHTM underscore the suitability of DHTM for long-term live imaging (40).

Here, we introduce DHTM to virus research by employing three different viruses, VACV of the *Poxviridae*, HSV-1 of the *Herpesviridae*, and RV from the *Picornaviridae*. VACV is an enveloped, double-stranded DNA virus, replicating and assembling particles in the cytoplasm (41). It is used to immunize and protect humans against smallpox caused by variola virus, one of the deadliest viruses to humans (42, 43). VACV exploits apoptotic mimicry to enter host cells through cellular blebbing, that is, protrusions of the cell membrane, implicated in cytokinesis and cell motility (20, 44, 45). VACV-

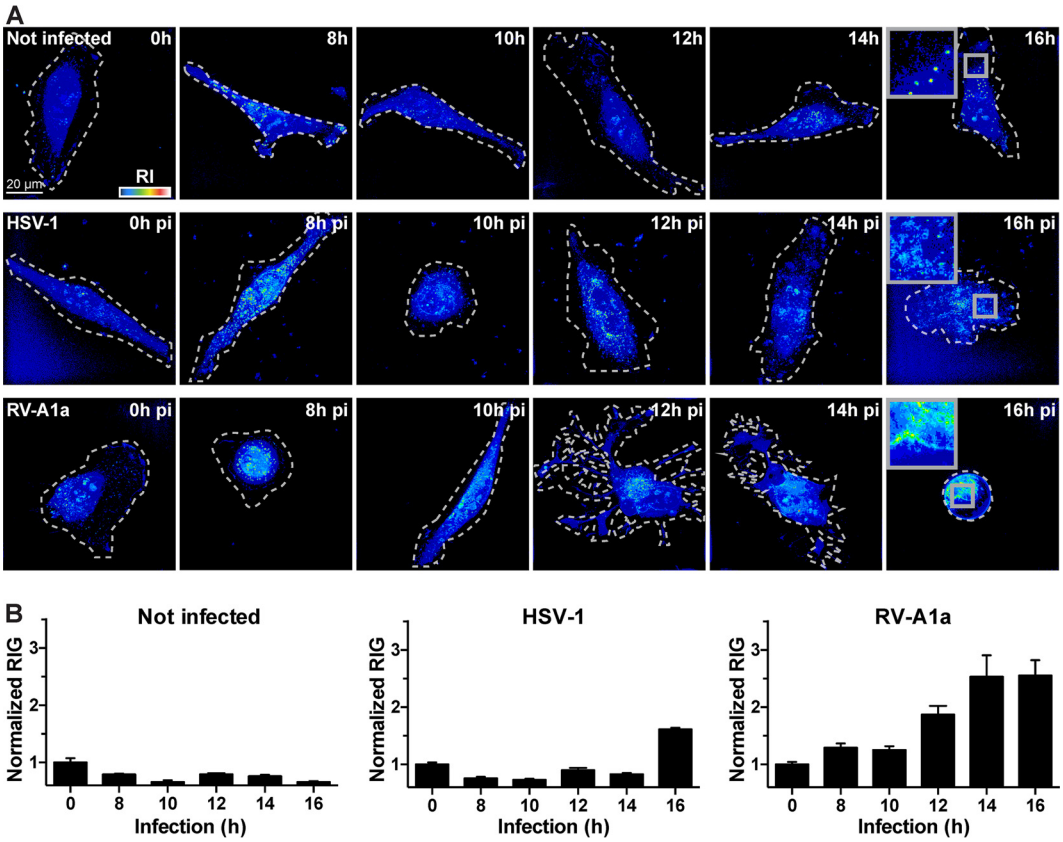

FIG 6 HSV-1 and RV increase cellular RIG late in infection. (A) Representative images of uninfected and infected cells imaged by a DHTM microscope at the indicated time points. HeLa-ATCC cells were infected with HSV-1-GFP (MOI of 10), and HeLa Ohio cells were infected with RV-A1a (MOI of 50). The perimeters of the cells grown on coverslips are outlined with white dashed lines, and the refractive indices are depicted as intensities in a "thermal" lookup table. Images were obtained as holograms, and the 3D stacks are depicted as z-projections of maxima. Bars, 20 μm. (B) Normalized cell RIG of the data shown in panel A. Bars depict mean values $\pm$ SEM of at least 10 cells for each condition and time point.

induced morphological changes of host cells include cell rounding, blebbing, and bud-like swellings (18). Picornaviruses are small, positive-sense single-stranded RNA viruses with a nonenveloped icosahedral capsid of 28 to 30 nm in diameter (46). RVs replicate in the cytoplasm on Golgi-derived membranes that are closely associated with the ER, and elicit a strong CPE in tissue culture (23–25). HSV-1 is an enveloped, double-stranded DNA virus, well adapted to human hosts and controlled by innate immunity, including the interferon-induced human myxovirus resistance protein B (MxB) (47). If HSV-1 breaks through the innate host defense, it replicates in the cell nucleus and sheds progeny prior to cell lysis (48, 49). In its latent state, HSV-1 evades the immune system, avoids CPE, and downregulates apoptosis (50, 51). Upon reactivation, HSV-1 is transmitted to the epidermal tissue where it causes lytic infection manifested as epidermal blisters.

We initially used DHTM to determine the volume of cells and became aware of periodic shrinkage and expansion of VACV-infected cells, as well as membrane blebbing at late stages of VACV infections, but not in RV-A1a infections. The cyclic volume changes observed by DHTM in VACV infections may be related to cellular contractility changes observed previously in VACV-infected cells, including cell rounding early and cell flattening late in infection (52). In pathology, cell volume dysregulation contributes to disorders, such as liver insufficiency, diabetic ketoacidosis, hypercatabolism, fibrosing disease, and sickle cell anemia, and regulation of cell volume affects cell proliferation and apoptosis (53). The VACV infection-induced cell volume oscillation implies that VACV regulates membrane trafficking, such as endocytosis and secretion, and possibly

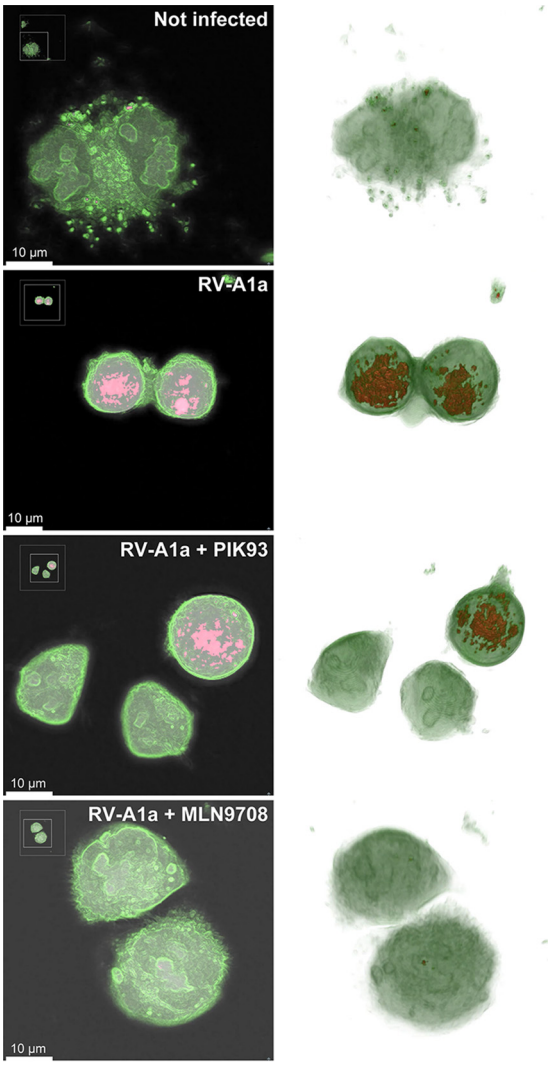

FIG 7 Drug treatment inhibits changes in RIs of RV-A1a-infected cells. Representative images of mock-infected (top panel) or RV-A1a-infected (MOI of 50) HeLa Ohio cells (lower three panels). Cells were treated with either PIK93 (5 μM), or MLN9708 (10 μM), and imaged by DHTM for 8 h at 1-min intervals. Cell membranes are labeled in green, high RI and RIG regions are shown in red. Images in the left column depict central z-slices of reconstructed holograms, and the images in the right column are 3D reconstructions of the holograms. See also Videos S4 to S7. Bars, 10 μm.

also ion channels. For example, the release of potassium, chloride, and bicarbonate ions is known to trigger cell shrinkage, or the accumulation of sodium, potassium, and chloride ions causes cell swelling through the activation of cotransporters, exchangers, or channel proteins (53). In addition, shrinkage and swelling processes involve organic osmolytes, such as sorbitol and glycerophosphorylcholine, which accumulate in shrinking cells and are released in swelling cells. How exactly VACV controls these processes remains an open question.

In addition to the accurate, noninvasive readout of cell volume, the RIGs measured by DHTM have served as an indicator for the granularity of cell structures (54). We show that specific RIG signatures indicate virus-induced CPEs. CPE follows cell shrinkage and blebbing and terminates in cell death (12, 55). In fact, viruses control cell death processes, including apoptosis or necroptosis, for example by diverting upstream regulating kinases, such as RIPK1 in RV-infected cells (1, 23). Other viruses prevent infection-induced apoptosis at early stages, gaining crucial time for production of virus progeny (50, 56–58). At late infection stages, viruses gain virulence by enhancing

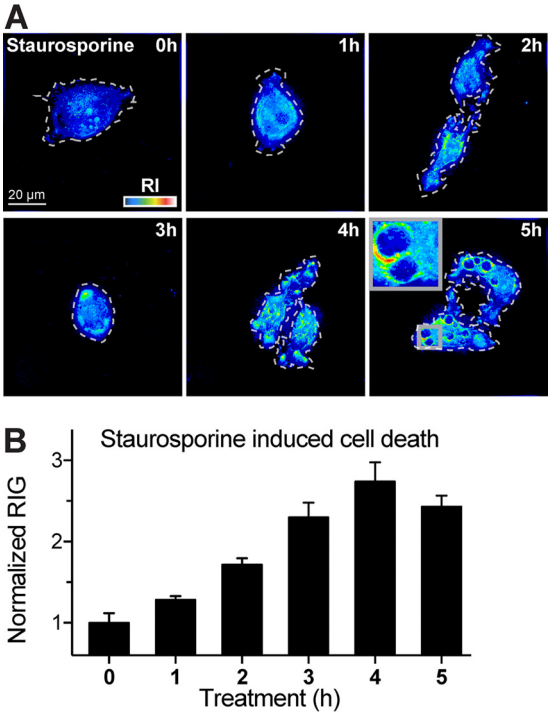

FIG 8 Staurosporine-induced apoptosis rapidly increases the cellular RIG. (A) Representative DHTM images of HeLa-Ohio cells incubated with staurosporine (10 μM) at 37°C for 5 h. Cell perimeters on the glass coverslip are outlined with white dashed lines, and RIs are depicted as intensities in the "thermal" lookup table. Images were obtained as holograms, and the 3D stacks are depicted as z-projections of maxima. Bar, 20 μm. (B) Cell RIG quantification of panel A. RIG values were normalized to 1 at 0 h after the addition. Bars depict mean values ± SEM of at least 10 cells for each condition and time.

progeny virus release from the cells (56, 59, 60). This leads to the notion that lytic infection resembles a necrosis-like program, leading to the release of both cellular contents and virus particles (7, 61).

CPEs are elicited not only by a wide range of pathogens, including viruses and bacteria, but they also emerge in malignant cells during transformation and in immune defense by cytotoxic cells for instance (6). Despite such insights, the CPE has remained one of the least understood processes in infection biology and pathology. This is in part due to the fact that a plethora of virus-induced cell reactions tune the infection, including proviral and antiviral signaling and innate immunity response. CPE arises as a result of the many altered processes in an infected cell. It is triggered by a few viral genes introduced into a naive cell and comprises proviral and antiviral components. Our results show that all viruses tested, VACV, HSV-1, and RV-A1a, induced RIG increase over the course of infection, with virus-specific kinetics, extent, and signature. Importantly, the RIG measurements scored CPE independent of cell contractions and blebbing, which cannot be uncoupled in phase-contrast microscopy. This indicates that RIG truly measures new dimensions in CPE that have not been accessible with conventional microscopy analyses. It underlines the superiority of DHTM over phase-contrast microscopy and allows the attribution of virus-specific processes to CPE. In the case of VACV infection, the RIG increase appeared to require late viral gene expression, since RIG changes were impaired by AraC, which inhibits late genes but not intermediate or early genes. For RV, we infer that at the onset of RIG increase at 8 h pi, not only are cytoplasmic membranes being rearranged and expanded for viral replication but also phase separation processes occur in the perinuclear area, a hallmark of RV-infected cells. In the case of HSV-1, the RIG increase was most dramatic at 16 h pi, with large changes in the nucleus and the cytoplasm, indicative of processes associated with virion production and release from the infected cell.

In conclusion, we show that DHTM is suitable to analyze cell biological processes in virus-infected cells at high spatiotemporal resolution, without the need to introduce cell markers or use high-intensity laser light. DHTM has high spatial resolution with potential superresolution options (35, 62). It enhances insights into CPE, a complex phenotype induced by nearly all pathogens, and increasingly mined by high-throughput screening assays (63). DHTM promotes the dynamic analyses of virus assembly, for example in phase separated zones of the cytoplasm and the nucleus, and provides a deeper understanding of the nature of viruses.

While the current state of DHTM technology has provided novel insights into virus-host interactions, the current technology has some limitations. For example, the correlative fluorescence-RI images provided in Fig. 1 are still images acquired with a prototype system and manual image acquisition. An automated stage would increase the statistical power and enable analyses of cell-to-cell variability, for example in correlation with virus replication kinetics and host factor contributions. Simultaneous video acquisition and RI analyses would further facilitate a broad-scale assessment of volume changes of whole cells or subcellular structures. Software implementations allowing for noninvasive simultaneous imaging of multiple cells could enhance the throughput of the technology. Collectively, this may enable future studies to test scenarios, such as how the expression kinetics of viral genes affect RI and RIG or how apoptosis and necrosis induction correlate with commonly used fluorescence markers.

MATERIALS AND METHODS

Cell lines and viruses. HeLa-ATCC cells from the American Type Culture Collection (ATCC) were maintained in Dulbecco modified Eagle medium (DMEM) (GIBCO-BRL) containing 10% fetal calf serum (FCS), nonessential amino acids (NEAA), and penicillin-streptomycin (GIBCO-BRL) at 37°C and 5% CO_2. All cell cultures were maintained in a cell bank system and kept at low passage numbers for all experiments.

Vaccinia virus strain International Health Department J (VACV-IHD-J) containing early/late (E/L) GFP transgene was kindly provided by J. Mercer (University College London, United Kingdom) (17, 64). To obtain the purified mature virions (MVs), cytoplasmic lysates were pelleted through a 36% sucrose cushion for 90 min with Optima XPN-100 ultracentrifuge (Beckmann Coulter) SW32Ti rotor at 18,000 rpm. The viral pellet was suspended in 10 mM Tris (pH 9.0), and virus was separated from contaminating material on a 25% to 40% sucrose gradient at 14,000 rpm for 45 min. Following centrifugation, the viral band was collected by aspiration and concentrated by pelleting at 14,000 rpm for 45 min. MVs were suspended in 1 mM Tris-HCl (pH 9.0), and the titers of virus were determined (titers in plaque-forming units [PFU] per milliliter) as previously described (65).

RVs were grown in HeLa cells as described previously (66, 67). Cells were inoculated with a lysate from infected cells at 33.5°C overnight. When CPE was visible in 80 to 90% of the cells, the medium was removed, and cells were harvested by scraping and pelleting. Cells were lysed by three freeze/thaw cycles in liquid nitrogen, followed by the addition of 1% NP-40 and homogenization with a Dounce homogenizer. The suspension was centrifuged at $2,500 \times g$ for 10 min, and the supernatant was transferred into a new tube. Free RNA was digested by the addition of 150 μg RNase per 10 ml and incubation at 37°C for 30 min. Virus was purified on a CsCl gradient and extensively dialyzed against 140 mM NaCl, 25 mM HEPES, and 5 mM $MgCl_2$.

The HSV-1 recombinant strain C12 expressing GFP from the major CMV promoter was kindly provided by S. Efstathiou (University of Cambridge, Cambridge, UK), and used as described previously (47, 68). All virus stocks were stored at −80°C. Infectivity of virus stocks was quantified by high-throughput fluorescence microscopy to determine the amount of inoculum resulting in >95% infected cells. From this, we calculated the MOI based on successful spreading events in plaque titration or $TCID_{50}$ experiments. VACV was titered on HeLa-ATCC cells, RV on HeLa-OHIO, and HSV-1 on A549-ATCC cells, according to earlier protocols (67). Virus-specific MOIs were calculated with $TCID_{50}$s by the Reed-Muench method (69). Note that VACV has an almost 1:1 ratio between early gene expression and spreading infections, while RV has significantly lower frequencies of virus spreading.

Cold-synchronized infections. Virus inocula were diluted into HEPES-buffered RPMI (Sigma) containing 10% FCS, NEAA, and penicillin-streptomycin (GIBCO-BRL), added to HeLa cells, and incubated on ice for 30 min. Enough virus was used to infect >95% cells in each of the DHTM experiments. Unbound virus was washed off three times with cold phosphate-buffered saline (PBS) and overlaid with either 37°C warm carbonate-buffered DMEM (GIBCO-BRL) containing 10% FCS, NEAA, and penicillin-streptomycin, or warm HEPES-buffered RPMI (Sigma) containing 10% FCS, nonessential amino acids, and penicillin-streptomycin for automated microscopy or tomographic holography, respectively.

Automated time-lapse, multisite, multichannel microscopy. Time-lapse, multisite, multichannel microscopy on HeLa cells grown in 96-well imaging plates (Greiner Bio-One) was performed with an ImageXpress Micro wide-field high-content analysis system (IXM-XL; Molecular Devices) microscope with a synthetic air-to-CO_2 mixture of 95% to 5%, respectively, in a humidified environment at 37°C with a 20× objective.

Live label-free holographic tomography. Live holographic tomography was performed using a 3D Cell Explorer microscope (Nanolive SA, Ecublens, Switzerland). Cells were grown and imaged using 35-mm Ibidi glass bottom μ-Dish dishes (Ibidi GmbH, Germany). During imaging, temperature (37°C) and humidity were controlled using an Ibidi Heating & Incubation System (Ibidi GmbH, Germany), while the pH was maintained by using RPMI containing 20 mM HEPES buffer.

Cell tracking and volume measurement. To measure the cell volume, 3D stacks obtained by DHTM were digitally stained and voxel segmented using STEVE (Nanolive SA, Ecublens, Switzerland), exported as TIF files, and imported into Imaris (Bitplane AG, Switzerland). Next, a surface was fitted to the imported 3D voxels aimed at complete volume segmentation. The fitted surface was tracked and enclosed features (volume, centroid position, and centroid speed) were measured with Imaris over the entire duration of the time-lapse experiment. Finally, the volume of each cell in a time-lapse series was normalized to the cell volume at time zero.

To benchmark the volume measurements from holographic tomography, we used polystyrene beads with diameters of 0.5, 0.75, and 1 μm (Fluoresbrite; Polysciences) and 4 μm (Tetraspeck; ThermoFisher). The beads were diluted in PBS, allowed to sediment to the bottom of the dish, and imaged. We next quantified their volume either by voxel segmentation and counting in STEVE or by surface fitting in Imaris (Fig. 4).

Cell refractive index gradient measurement. The RI of a material is defined as speed of light in vacuum divided by the speed of light in the particular material. RIG is a computed value describing RI change within a neighborhood of a particular voxel according to the following equation:

$$\mathrm{RIG} = \sqrt{\left(\frac{\mathrm{RI}_{x+1,y,z} - \mathrm{RI}_{x-1,y,z}}{2p_x}\right)^2 + \left(\frac{\mathrm{RI}_{x,y+1,z} - RI_{x,y-1,z}}{2p_y}\right)^2 + \left(\frac{\mathrm{RI}_{x,y,z+1} - \mathrm{RI}_{x,y,z-1}}{2p_z}\right)^2} \quad (1)$$

where $2p_x$, $2p_y$, and $2p_z$ are the resolution of the image, and $\mathrm{RI}_{x\pm1,y\pm1,z\pm1}$ is the RI value of the neighboring pixels.

Measurement of the relative RIG of the cells was performed by "digital staining" in STEVE according to the user manual. The staining was aimed at segmenting at least 95% of the manually determined cellular signal; next, the mean RIG of the digital staining was calculated. Boundaries were adjusted by shifting the RI outside of the 95% constraint. Finally, RIG of each cell in a time-lapse experiment was normalized to the RIG of the cell at the start of the time-lapse experiment.

Data availability. Scripts, data, and further materials can be downloaded from the GitHub repository at https://github.com/ayakimovich/DHMViruses.

SUPPLEMENTAL MATERIAL

Supplemental material for this article may be found at https://doi.org/10.1128/mSphereDirect.00599-18.

VIDEO S1, MOV file, 5.6 MB.
VIDEO S2, MOV file, 1.5 MB.
VIDEO S3, MOV file, 2.2 MB.
VIDEO S4, MOV file, 8.8 MB.
VIDEO S5, MOV file, 5 MB.
VIDEO S6, MOV file, 8.1 MB.
VIDEO S7, MOV file, 7.7 MB.
FIG S1, TIF file, 2.1 MB.

ACKNOWLEDGMENTS

We thank all members of the Greber lab for discussions and comments throughout the course of this work. We thank Nicole Meili and Melanie Grove for tissue culture and general lab support. We acknowledge excellent technical support from Lisa Pollaro, Luca Clario, and Sorin Pop (Nanolive SA, Ecublens, Switzerland). We thank the Center for Microscopy and Image Analysis at the University of Zurich headed by Urs Ziegler for providing polystyrene beads. We thank Jason Mercer (MRC LMCB, University College London, London, United Kingdom) for kindly providing vaccinia virus IHD-J E/L-GFP.

This work was supported by the University of Zurich and by grants to U.F.G. from the Swiss Initiative in Systems Biology (SystemsX.ch) (VirX) and the Swiss National Science Foundation (grants 310030B_160316 and 31003A_179256/1).

U.F.G., A.Y., R.W., and V.A. initiated the study and designed experiments. A.Y., R.W., V.A., and F.G. performed and analyzed the experiments. A.Y., R.W., and V.A. developed analysis algorithms. R.W., A.Y., and U.F.G. wrote the manuscript with input from V.A. and F.G.

We declare that we have no conflicts of interest.

REFERENCES

1. Mocarski ES, Upton JW, Kaiser WJ. 2012. Viral infection and the evolution of caspase 8-regulated apoptotic and necrotic death pathways. Nat Rev Immunol 12:79–88. https://doi.org/10.1038/nri3131.
2. Agol VI. 2012. Cytopathic effects: virus-modulated manifestations of innate immunity? Trends Microbiol 20:570–576. https://doi.org/10.1016/j.tim.2012.09.003.
3. Rubbia-Brandt L, Quadri R, Abid K, Giostra E, Male PJ, Mentha G, Spahr L, Zarski JP, Borisch B, Hadengue A, Negro F. 2000. Hepatocyte steatosis is a cytopathic effect of hepatitis C virus genotype 3. J Hepatol 33:106–115. https://doi.org/10.1016/S0168-8278(00)80166-X.
4. Perng GC, Jones C, Ciacci-Zanella J, Stone M, Henderson G, Yukht A, Slanina SM, Hofman FM, Ghiasi H, Nesburn AB, Wechsler SL. 2000. Virus-induced neuronal apoptosis blocked by the herpes simplex virus latency-associated transcript. Science 287:1500–1503. https://doi.org/10.1126/science.287.5457.1500.
5. Rhoades RE, Tabor-Godwin JM, Tsueng G, Feuer R. 2011. Enterovirus infections of the central nervous system. Virology 411:288–305. https://doi.org/10.1016/j.virol.2010.12.014.
6. Heaton NS. 2017. Revisiting the concept of a cytopathic viral infection. PLoS Pathog 13:e1006409. https://doi.org/10.1371/journal.ppat.1006409.
7. Yakimovich A, Gumpert H, Burckhardt CJ, Lutschg VA, Jurgeit A, Sbalzarini IF, Greber UF. 2012. Cell-free transmission of human adenovirus by passive mass transfer in cell culture simulated in a computer model. J Virol 86:10123–10137. https://doi.org/10.1128/JVI.01102-12.
8. Zheng Y, Stamminger T, Hearing P. 2016. E2F/Rb family proteins mediate interferon induced repression of adenovirus immediate early transcription to promote persistent viral infection. PLoS Pathog 12:e1005415. https://doi.org/10.1371/journal.ppat.1005415.
9. Thompson CB. 1995. Apoptosis in the pathogenesis and treatment of disease. Science 267:1456–1462. https://doi.org/10.1126/science.7878464.
10. Chiou SK, White E. 1998. Inhibition of ICE-like proteases inhibits apoptosis and increases virus production during adenovirus infection. Virology 244:108–118. https://doi.org/10.1006/viro.1998.9077.
11. Wang Z, Xia X, Yang X, Zhang X, Liu Y, Wu D, Fang Y, Liu Y, Xu J, Qiu Y, Zhou X. 2017. A picorna-like virus suppresses the N-end rule pathway to inhibit apoptosis. Elife 6:e30590. https://doi.org/10.7554/eLife.30590.
12. Pereira HG. 1961. The cytopathic effect of animal viruses. Adv Virus Res 8:245–285.
13. Netherton C, Moffat K, Brooks E, Wileman T. 2007. A guide to viral inclusions, membrane rearrangements, factories, and viroplasm produced during virus replication. Adv Virus Res 70:101–182. https://doi.org/10.1016/S0065-3527(07)70004-0.
14. Allen RD. 1985. New observations on cell architecture and dynamics by video-enhanced contrast optical microscopy. Annu Rev Biophys Biophys Chem 14:265–290. https://doi.org/10.1146/annurev.bb.14.060185.001405.
15. Cotte Y, Toy F, Jourdain P, Pavillon N, Boss D, Magistretti P, Marquet P, Depeursinge C. 2013. Marker-free phase nanoscopy. Nat Photonics 7:113–117. https://doi.org/10.1038/nphoton.2012.329.
16. Schabel FM, Jr. 1968. The antiviral activity of 9-beta-D-arabinofuranosyladenine (ARA-A). Chemotherapia (Basel) 13:321–338. https://doi.org/10.1159/000220567.
17. Yakimovich A, Huttunen M, Zehnder B, Coulter LJ, Gould V, Schneider C, Kopf M, McInnes CJ, Greber UF, Mercer J. 2017. Inhibition of poxvirus gene expression and genome replication by bisbenzimide derivatives. J Virol 91:e00838-17. https://doi.org/10.1128/JVI.00838-17.
18. Gamliel H, Polliack A, Sarov I. 1977. Surface features of vaccinia virus-infected human embryonic cells as studied by scanning electron microscopy. Virology 83:195–203. https://doi.org/10.1016/0042-6822(77)90222-7.
19. Charras GT, Hu CK, Coughlin M, Mitchison TJ. 2006. Reassembly of contractile actin cortex in cell blebs. J Cell Biol 175:477–490. https://doi.org/10.1083/jcb.200602085.
20. Mercer J, Helenius A. 2008. Vaccinia virus uses macropinocytosis and apoptotic mimicry to enter host cells. Science 320:531–535. https://doi.org/10.1126/science.1155164.
21. Seipelt J, Liebig HD, Sommergruber W, Gerner C, Kuechler E. 2000. 2A proteinase of human rhinovirus cleaves cytokeratin 8 in infected HeLa cells. J Biol Chem 275:20084–20089. https://doi.org/10.1074/jbc.275.26.20084.
22. Sobo K, Stuart AD, Rubbia-Brandt L, Brown TD, McKee TA. 2012. Echovirus 11 infection induces dramatic changes in the actin cytoskeleton of polarized Caco-2 cells. J Gen Virol 93:475–487. https://doi.org/10.1099/vir.0.037697-0.
23. Lotzerich M, Roulin PS, Boucke K, Witte R, Georgiev O, Greber UF. 2018. Rhinovirus 3C protease suppresses apoptosis and triggers caspase-independent cell death. Cell Death Dis 9:272. https://doi.org/10.1038/s41419-018-0306-6.
24. Roulin PS, Lotzerich M, Torta F, Tanner LB, van Kuppeveld FJ, Wenk MR, Greber UF. 2014. Rhinovirus uses a phosphatidylinositol 4-phosphate/cholesterol counter-current for the formation of replication compartments at the ER-Golgi interface. Cell Host Microbe 16:677–690. https://doi.org/10.1016/j.chom.2014.10.003.
25. Belov GA. 2016. Dynamic lipid landscape of picornavirus replication organelles. Curr Opin Virol 19:1–6. https://doi.org/10.1016/j.coviro.2016.05.003.
26. Si X, McManus BM, Zhang J, Yuan J, Cheung C, Esfandiarei M, Suarez A, Morgan A, Luo H. 2005. Pyrrolidine dithiocarbamate reduces coxsackievirus B3 replication through inhibition of the ubiquitin-proteasome pathway. J Virol 79:8014–8023. https://doi.org/10.1128/JVI.79.13.8014-8023.2005.
27. Gao G, Zhang J, Si X, Wong J, Cheung C, McManus B, Luo H. 2008. Proteasome inhibition attenuates coxsackievirus-induced myocardial damage in mice. Am J Physiol Heart Circ Physiol 295:H401–H408. https://doi.org/10.1152/ajpheart.00292.2008.
28. Kupperman E, Lee EC, Cao Y, Bannerman B, Fitzgerald M, Berger A, Yu J, Yang Y, Hales P, Bruzzese F, Liu J, Blank J, Garcia K, Tsu C, Dick L, Fleming P, Yu L, Manfredi M, Rolfe M, Bolen J. 2010. Evaluation of the proteasome inhibitor MLN9708 in preclinical models of human cancer. Cancer Res 70:1970–1980. https://doi.org/10.1158/0008-5472.CAN-09-2766.
29. Roulin PS, Murer L, Greber UF. 2018. A single point mutation in the rhinovirus 2B protein reduces the requirement for phosphatidylinositol 4-kinase class III beta in viral replication. J Virol 92:e01462-18. https://doi.org/10.1128/JVI.01462-18.
30. Chae HJ, Kang JS, Byun JO, Han KS, Kim DU, Oh SM, Kim HM, Chae SW, Kim HR. 2000. Molecular mechanism of staurosporine-induced apoptosis in osteoblasts. Pharmacol Res 42:373–381. https://doi.org/10.1006/phrs.2000.0700.
31. Charriere F, Pavillon N, Colomb T, Depeursinge C, Heger TJ, Mitchell EA, Marquet P, Rappaz B. 2006. Living specimen tomography by digital holographic microscopy: morphometry of testate amoeba. Opt Express 14:7005–7013. https://doi.org/10.1364/OE.14.007005.
32. Lauer V. 2002. New approach to optical diffraction tomography yielding a vector equation of diffraction tomography and a novel tomographic microscope. J Microsc 205:165–176. https://doi.org/10.1046/j.0022-2720.2001.00980.x.
33. Montfort F, Charriere F, Colomb T, Cuche E, Marquet P, Depeursinge C. 2006. Purely numerical compensation for microscope objective phase curvature in digital holographic microscopy: influence of digital phase mask position. J Opt Soc Am A Opt Image Sci Vis 23:2944–2953. https://doi.org/10.1364/JOSAA.23.002944.
34. Paturzo M, Merola F, Grilli S, De Nicola S, Finizio A, Ferraro P. 2008. Super-resolution in digital holography by a two-dimensional dynamic phase grating. Opt Express 16:17107–17118. https://doi.org/10.1364/OE.16.017107.
35. Cotte Y, Toy MF, Pavillon N, Depeursinge C. 2010. Microscopy image resolution improvement by deconvolution of complex fields. Opt Express 18:19462–19478. https://doi.org/10.1364/OE.18.019462.
36. Sheppard CJ, Kou SS, Depeursinge C. 2012. Reconstruction in interferometric synthetic aperture microscopy: comparison with optical coherence tomography and digital holographic microscopy. J Opt Soc Am A Opt Image Sci Vis 29:244–250. https://doi.org/10.1364/JOSAA.29.000244.
37. Park Y, Diez-Silva M, Popescu G, Lykotrafitis G, Choi W, Feld MS, Suresh S. 2008. Refractive index maps and membrane dynamics of human red blood cells parasitized by Plasmodium falciparum. Proc Natl Acad Sci U S A 105:13730–13735. https://doi.org/10.1073/pnas.0806100105.
38. Witte R, Andriasyan V, Georgi F, Yakimovich A, Greber UF. 2018. Con-

cepts in light microscopy of viruses. Viruses 10:E202. https://doi.org/10.3390/v10040202.
39. Wang IH, Burckhardt CJ, Yakimovich A, Greber UF. 2018. Imaging, tracking and computational analyses of virus entry and egress with the cytoskeleton. Viruses 10:E166. https://doi.org/10.3390/v10040166.
40. Javidi B, Markman A, Rawat S, O'Connor T, Anand A, Andemariam B. 2018. Sickle cell disease diagnosis based on spatio-temporal cell dynamics analysis using 3D printed shearing digital holographic microscopy. Opt Express 26:13614–13627. https://doi.org/10.1364/OE.26.013614.
41. Moss B, Salzman NP. 1968. Sequential protein synthesis following vaccinia virus infection. J Virol 2:1016–1027.
42. Moss B. 2011. Smallpox vaccines: targets of protective immunity. Immunol Rev 239:8–26. https://doi.org/10.1111/j.1600-065X.2010.00975.x.
43. Harrison SC, Alberts B, Ehrenfeld E, Enquist L, Fineberg H, McKnight SL, Moss B, O'Donnell M, Ploegh H, Schmid SL, Walter KP, Theriot J. 2004. Discovery of antivirals against smallpox. Proc Natl Acad Sci U S A 101:11178–11192. https://doi.org/10.1073/pnas.0403600101.
44. Morales I, Carbajal MA, Bohn S, Holzer D, Kato SE, Greco FA, Moussatche N, Krijnse Locker J. 2008. The vaccinia virus F11L gene product facilitates cell detachment and promotes migration. Traffic 9:1283–1298. https://doi.org/10.1111/j.1600-0854.2008.00762.x.
45. Humphries AC, Way M. 2013. The non-canonical roles of clathrin and actin in pathogen internalization, egress and spread. Nat Rev Microbiol 11:551–560. https://doi.org/10.1038/nrmicro3072.
46. Rossmann MG, Arnold E, Erickson JW, Frankenberger EA, Griffith JP, Hecht HJ, Johnson JE, Kamer G, Luo M, Mosser AG, et al. 1985. Structure of a human common cold virus and functional relationship to other picornaviruses. Nature 317:145–153. https://doi.org/10.1038/317145a0.
47. Crameri M, Bauer M, Caduff N, Walker R, Steiner F, Franzoso FD, Gujer C, Boucke K, Kucera T, Zbinden A, Munz C, Fraefel C, Greber UF, Pavlovic J. 2018. MxB is an interferon-induced restriction factor of human herpesviruses. Nat Commun 9:1980. https://doi.org/10.1038/s41467-018-04379-2.
48. Yamauchi Y, Kiriyama K, Kimura H, Nishiyama Y. 2008. Herpes simplex virus induces extensive modification and dynamic relocalisation of the nuclear mitotic apparatus (NuMA) protein in interphase cells. J Cell Sci 121:2087–2096. https://doi.org/10.1242/jcs.031450.
49. Roizman B, Knipe DM, Whitley RJ. 2013. Herpes simplex viruses, p 1823–1897. *In* Knipe DM, Howley PM, Cohen JI, Griffin DE, Lamb RA, Martin MA, Racaniello VR, Roizman B (ed), Fields virology, 6th ed, vol 1. Lippincott Williams & Wilkins, Philadelphia, PA.
50. Leopardi R, Van Sant C, Roizman B. 1997. The herpes simplex virus 1 protein kinase US3 is required for protection from apoptosis induced by the virus. Proc Natl Acad Sci U S A 94:7891–7896. https://doi.org/10.1073/pnas.94.15.7891.
51. Gupta A, Gartner JJ, Sethupathy P, Hatzigeorgiou AG, Fraser NW. 2006. Anti-apoptotic function of a microRNA encoded by the HSV-1 latency-associated transcript. Nature 442:82–85. https://doi.org/10.1038/nature04836.
52. Schramm B, de Haan CA, Young J, Doglio L, Schleich S, Reese C, Popov AV, Steffen W, Schroer T, Locker JK. 2006. Vaccinia-virus-induced cellular contractility facilitates the subcellular localization of the viral replication sites. Traffic 7:1352–1367. https://doi.org/10.1111/j.1600-0854.2006.00470.x.
53. Lang F, Foller M, Lang K, Lang P, Ritter M, Vereninov A, Szabo I, Huber SM, Gulbins E. 2007. Cell volume regulatory ion channels in cell proliferation and cell death. Methods Enzymol 428:209–225. https://doi.org/10.1016/S0076-6879(07)28011-5.
54. Rappaz B, Marquet P, Cuche E, Emery Y, Depeursinge C, Magistretti P. 2005. Measurement of the integral refractive index and dynamic cell morphometry of living cells with digital holographic microscopy. Opt Express 13:9361–9373. https://doi.org/10.1364/OPEX.13.009361.
55. Coleman ML, Sahai EA, Yeo M, Bosch M, Dewar A, Olson MF. 2001. Membrane blebbing during apoptosis results from caspase-mediated activation of ROCK I. Nat Cell Biol 3:339–345. https://doi.org/10.1038/35070009.
56. Rao L, Debbas M, Sabbatini P, Hockenbery D, Korsmeyer S, White E. 1992. The adenovirus E1A proteins induce apoptosis, which is inhibited by the E1B 19-kDa and Bcl-2 proteins. Proc Natl Acad Sci U S A 89:7742–7746. https://doi.org/10.1073/pnas.89.16.7742.
57. Kettle S, Khanna A, Alcami A, Jassoy C, Ehret R, Smith GL. 1997. Vaccinia virus serpin B13R (SPI-2) inhibits interleukin-1beta-converting enzyme and protects virus-infected cells from TNF- and Fas-mediated apoptosis, but does not prevent IL-1beta-induced fever. J Gen Virol 78:677–685. https://doi.org/10.1099/0022-1317-78-3-677.
58. Kvansakul M, Yang H, Fairlie WD, Czabotar PE, Fischer SF, Perugini MA, Huang DC, Colman PM. 2008. Vaccinia virus anti-apoptotic F1L is a novel Bcl-2-like domain-swapped dimer that binds a highly selective subset of BH3-containing death ligands. Cell Death Differ 15:1564–1571. https://doi.org/10.1038/cdd.2008.83.
59. Chen W, Calvo PA, Malide D, Gibbs J, Schubert U, Bacik I, Basta S, O'Neill R, Schickli J, Palese P, Henklein P, Bennink JR, Yewdell JW. 2001. A novel influenza A virus mitochondrial protein that induces cell death. Nat Med 7:1306–1312. https://doi.org/10.1038/nm1201-1306.
60. Deszcz L, Gaudernak E, Kuechler E, Seipelt J. 2005. Apoptotic events induced by human rhinovirus infection. J Gen Virol 86:1379–1389. https://doi.org/10.1099/vir.0.80754-0.
61. Kaczmarek A, Vandenabeele P, Krysko DV. 2013. Necroptosis: the release of damage-associated molecular patterns and its physiological relevance. Immunity 38:209–223. https://doi.org/10.1016/j.immuni.2013.02.003.
62. Mico V, Zalevsky Z, Ferreira C, Garcia J. 2008. Superresolution digital holographic microscopy for three-dimensional samples. Opt Express 16:19260–19270. https://doi.org/10.1364/OE.16.019260.
63. McCormick KD, Liu S, Jacobs JL, Marques ET, Jr, Sluis-Cremer N, Wang T. 2012. Development of a robust cytopathic effect-based high-throughput screening assay to identify novel inhibitors of dengue virus. Antimicrob Agents Chemother 56:3399–3401. https://doi.org/10.1128/AAC.06425-11.
64. Mercer J, Knebel S, Schmidt FI, Crouse J, Burkard C, Helenius A. 2010. Vaccinia virus strains use distinct forms of macropinocytosis for host-cell entry. Proc Natl Acad Sci U S A 107:9346–9351. https://doi.org/10.1073/pnas.1004618107.
65. Mercer J, Traktman P. 2003. Investigation of structural and functional motifs within the vaccinia virus A14 phosphoprotein, an essential component of the virion membrane. J Virol 77:8857–8871. https://doi.org/10.1128/JVI.77.16.8857-8871.2003.
66. Jurgeit A, Moese S, Roulin P, Dorsch A, Lotzerich M, Lee WM, Greber UF. 2010. An RNA replication-center assay for high content image-based quantifications of human rhinovirus and coxsackievirus infections. Virol J 7:264. https://doi.org/10.1186/1743-422X-7-264.
67. Jurgeit A, McDowell R, Moese S, Meldrum E, Schwendener R, Greber UF. 2012. Niclosamide is a proton carrier and targets acidic endosomes with broad antiviral effects. PLoS Pathog 8:e1002976. https://doi.org/10.1371/journal.ppat.1002976.
68. Glauser DL, Seyffert M, Strasser R, Franchini M, Laimbacher AS, Dresch C, de Oliveira AP, Vogel R, Buning H, Salvetti A, Ackermann M, Fraefel C. 2010. Inhibition of herpes simplex virus type 1 replication by adeno-associated virus Rep proteins depends on their combined DNA-binding and ATPase/helicase activities. J Virol 84:3808–3824. https://doi.org/10.1128/JVI.01503-09.
69. Reed L, Muench H. 1938. A simple method of estimating fifty per cent endpoints. Am J Epidemiol 27:493–497. https://doi.org/10.1093/oxfordjournals.aje.a118408.